

RESEARCH ARTICLE**Conservative discontinuous Galerkin method for supercritical, real-fluid flows**

Eric J. Ching | Ryan F. Johnson

arXiv:2410.13810v2 [physics.flu-dyn] 21 Oct 2024

¹Laboratories for Computational Physics and Fluid Dynamics, U.S. Naval Research Laboratory, 4555 Overlook Ave SW, Washington, DC 20375

Correspondence

*Eric Ching, Email:
eric.j.ching.civ@us.navy.mil

This paper presents a conservative discontinuous Galerkin method for the simulation of supercritical and transcritical real-fluid flows without phase separation. A well-known issue associated with the use of fully conservative schemes is the generation of spurious pressure oscillations at contact interfaces, which are exacerbated when a cubic equation of state and thermodynamic relations appropriate for this high-pressure flow regime are considered. To reduce these pressure oscillations, which can otherwise lead to solver divergence in the absence of additional dissipation, an L^2 -projection of primitive variables is performed in the evaluation of the flux. We apply the discontinuous Galerkin formulation to a variety of test cases. The first case is the advection of a sinusoidal density wave, which is used to verify the convergence of the scheme. The next two involve one- and two-dimensional advection of a nitrogen/n-dodecane thermal bubble, in which the ability of the methodology to reduce pressure oscillations and maintain solution stability is assessed. The final test cases consist of two- and three-dimensional injection of an n-dodecane jet into a nitrogen chamber.

KEYWORDS:

Discontinuous Galerkin method; Supercritical flow; Transcritical flow; Spurious pressure oscillations

1 | INTRODUCTION

Supercritical and transcritical flows are important in a variety of engineering applications. For instance, in rocket engines, gas turbines, and diesel engines, the fuel is often injected at high pressures to improve engine efficiency and reduce emissions [1]. In supercritical injection, the fuel is injected at a supercritical temperature. On the other hand, in transcritical injection, the fuel is injected at a subcritical temperature and then heated to supercritical temperatures prior to combustion. Many of the relevant physical phenomena characterizing these flows are not observed in subcritical systems. For example, thermodynamic gradients are substantial, the liquid-gas phase boundary begins to vanish (although phase separation may still occur in certain transcritical flows), and surface tension may no longer play an important role. Although various studies have been conducted to investigate supercritical and transcritical flows, significant gaps in understanding of these flows still exist.

Computational fluid dynamics (CFD) can help close these gaps, with diffuse-interface methods commonly employed to simulate supercritical and transcritical flows; however, certain numerical challenges hinder the reliability of CFD for providing detailed insights into the relevant physics. For instance, cubic or tabulated equations of state are often employed, which increase complexity and can result in the loss of certain desirable physical and mathematical properties associated with the ideal-gas equation of state. Furthermore, the large density gradients that exist between the gas-like and liquid-like phases easily lead to

numerical instabilities and potentially solver divergence. One of the most prominent numerical challenges is the generation of spurious pressure oscillations when fully conservative schemes are employed. Commonly discussed in the context of multi-component, ideal-gas flows [2], this issue is caused by the loss of mechanical equilibrium at contact interfaces due to variable thermodynamic properties, which is further exacerbated by the increased nonlinearity associated with supercritical and trans-critical flows. In the absence of appropriate numerical treatment, these spurious pressure oscillations can grow rapidly and lead to solver divergence. A number of quasi-conservative schemes have been developed to circumvent this problem. For instance, a pressure evolution equation can be solved instead of the total-energy equation to maintain pressure equilibrium [3]. The double-flux scheme [4], which freezes the thermodynamics elementwise and recasts the equation of state in a calorically-perfect form, is another popular option. It was first developed for multicomponent, ideal-gas flows and was later extended to transcritical flows [5]. However, the loss of energy conservation in these quasi-conservative schemes is undesirable. To mitigate (but not eliminate) the conservation error, Boyd and Jarrahbashi [6] developed a hybrid scheme that switches between the double-flux method and a fully conservative method according to the jump in certain thermodynamic quantities.

Finite-difference and finite-volume schemes comprise the majority of numerical techniques for simulating supercritical flows. The discontinuous Galerkin (DG) method is a promising alternative due to its arbitrarily high order of accuracy, compact stencil, geometric flexibility, compatibility with local adaptivity, and amenability to modern computing architectures [7]. Apart from a handful of approaches in the literature [8, 9], DG-based formulations for transcritical and supercritical flows are very limited. Given the advantages offered by DG schemes, the main objectives of this work are to present a fully conservative DG formulation [10, 11] for supercritical and transcritical flows (without phase separation) and assess its ability to accurately and robustly simulate flows in this regime. This formulation was originally developed to simulate multicomponent, chemically reacting flows involving mixtures of thermally perfect gases [10]. It was found that using a colocated scheme, pressure equilibrium was successfully maintained (in an approximate sense) in the one-dimensional advection of a hydrogen/oxygen thermal bubble. Although pressure oscillations were present, they remained small throughout the simulation. In contrast, with standard overintegration, pressure oscillations grew rapidly and caused solver divergence. To maintain solution stability while employing overintegration, the authors introduced an overintegration strategy in which the pressure is projected onto the finite element test space via interpolation [10]. Bando [12] further assessed this overintegration strategy and compared it to a modified strategy, inspired by a similar approach by Franchina et al. [13], in which the pressure is projected instead via L^2 -projection. Using the same hydrogen/oxygen thermal-bubble configuration as a test bed, it was concluded that although both approaches maintained approximate pressure equilibrium, the interpolation-based approach is preferred since it is simpler and yielded smaller pressure oscillations. However, it was recently found that in a more challenging test case involving the one-dimensional advection of a high-pressure, nitrogen/n-dodecane thermal bubble (which is more representative of realistic transcritical/supercritical flows even though the thermally perfect gas model was employed), the L^2 -projection-based overintegration strategy significantly improved solution stability [11]. Here, we evaluate whether this overintegration strategy can similarly maintain solution stability when real-fluid effects in multiple dimensions are considered.

The remainder of this paper is organized as follows. Sections 2 and 3 summarize the governing equations and DG formulation, respectively. Results for a variety of test cases, including multidimensional advection of a nitrogen/n-dodecane thermal bubble and injection of an n-dodecane jet into a nitrogen chamber, are given in the following section. We close the paper with concluding remarks.

2 | GOVERNING EQUATIONS

The governing equations for conservation of species concentrations, momentum, and total energy are written as

$$\frac{\partial \mathbf{y}}{\partial t} + \nabla \cdot \mathcal{F}(\mathbf{y}) = 0, \quad (2.1)$$

where \mathbf{y} is the vector of m state variables, t is time, and \mathcal{F} is the convective flux. The physical coordinates are denoted by $\mathbf{x} = (x_1, \dots, x_d)$, where d is the number of spatial dimensions. The state vector is expanded as

$$\mathbf{y} = (\rho v_1, \dots, \rho v_d, \rho e_t, C_1, \dots, C_{n_s})^T, \quad (2.2)$$

where ρ is the density, $v = (v_1, \dots, v_d)$ is the velocity vector, e_t is the specific total energy, $C = (C_1, \dots, C_{n_s})$ is the vector of molar concentrations, and n_s is the number of species. The density can be computed as

$$\rho = \sum_{i=1}^{n_s} \rho_i = \sum_{i=1}^{n_s} W_i C_i,$$

where ρ_i and W_i are the partial density and molecular weight, respectively, of the i th species. The mole and mass fractions of the i th species are given by

$$X_i = \frac{C_i}{\sum_{i=1}^{n_s} C_i}, \quad Y_i = \frac{\rho_i}{\rho}.$$

The specific total energy is expanded as

$$e_t = u + \frac{1}{2} \sum_{k=1}^d v_k v_k,$$

where u is the mixture-averaged specific internal energy, computed as the mass-weighted sum of the specific internal energies of each species, i.e.,

$$u = \sum_{i=1}^{n_s} Y_i u_i.$$

The k th spatial component of the convective flux is given by

$$\mathcal{F}_k(y) = (\rho v_k v_1 + P \delta_{k1}, \dots, \rho v_k v_d + P \delta_{kd}, v_k (\rho e_t + P), v_k C_1, \dots, v_k C_{n_s})^T, \quad (2.3)$$

where P is the pressure, which is computed using the Peng-Robinson cubic equation of state [14]:

$$P = \frac{\hat{R}T}{\hat{v} - b} - \frac{a\alpha}{\hat{v}^2 + 2b\hat{v} - b^2}. \quad (2.4)$$

T is the temperature, $\hat{v} = 1 / \sum_{i=1}^{n_s} C_i$ is the molar volume, $a\alpha$ and b are the attractive and repulsive parameters, respectively, and \hat{R} is the universal gas constant. To further account for real-fluid effects, thermodynamic quantities are computed by augmenting the NASA-polynomial-based ideal-gas values [15, 16] with departure functions, which, in the case of mixtures, are evaluated using the extended corresponding states principle and pure-fluid assumption [17, 18] and the recommended mixing rules by Harstad et al. [19]. More information on the exact forms of the departure functions for a generic cubic equation of state can be found in Appendix A. As in [6], viscous effects are ignored here since they are not the cause of spurious pressure oscillations. Surface tension is also neglected, which is typical for supercritical/transcritical flow models [5, 6, 20]. Table 1 lists the critical properties of the species considered in Section 4.

TABLE 1 Relevant properties of the species considered in this paper. W is the molecular mass, $(\cdot)_c$ denotes critical property, and ω is the acentric factor.

Species	W (kg/kmol)	T_c (K)	P_c (MPa)	ρ_c (kg/m ³)	ω
N ₂	28.0	126.2	3.40	313.3	0.0372
<i>n</i> -C ₁₂ H ₂₆	170.3	658.1	1.82	226.5	0.574

A well-known issue with the Peng-Robinson equation of state is that it returns negative pressure and complex sound speed under certain conditions. Given the flows targeted in this study (i.e., no phase separation), such conditions are obtained typically as a result of numerical instabilities, in which case we limit the pressure and speed of sound returned by the equation of state to minimum values of 10 Pa and 1 m/s, respectively. More sophisticated modifications can also be employed [6, 21].

3 | DISCONTINUOUS GALERKIN DISCRETIZATION

Let Ω denote the computational domain partitioned by \mathcal{T} , which consists of cells κ with boundaries $\partial\kappa$. Let \mathcal{E} denote the set of interfaces ϵ , consisting of the interior interfaces,

$$\epsilon_I \in \mathcal{E}_I = \{\epsilon_I \in \mathcal{E} \mid \epsilon_I \cap \partial\Omega = \emptyset\},$$

and boundary interfaces,

$$\epsilon_\partial \in \mathcal{E}_\partial = \{\epsilon_\partial \in \mathcal{E} \mid \epsilon_\partial \subset \partial\Omega\}.$$

At interior interfaces, there exist κ^+ and κ^- such that $\epsilon_I = \partial\kappa^+ \cap \partial\kappa^-$. n^+ and n^- denote the outward facing normals of κ^+ and κ^- , respectively. Let V_h^p denote the space of test and basis functions

$$V_h^p = \{\mathbf{v} \in [L^2(\Omega)]^m \mid \forall \kappa \in \mathcal{T}, \mathbf{v}|_\kappa \in [\mathcal{P}_p(\kappa)]^m\}, \quad (3.1)$$

where $\mathcal{P}_p(\kappa)$ is a space of polynomial functions of degree no greater than p in κ .

The semi-discrete form of Equation (2.1) is as follows: find $y \in V_h^p$ such that

$$\sum_{\kappa \in \mathcal{T}} \left(\frac{\partial y}{\partial t}, \mathbf{v} \right)_\kappa - \sum_{\kappa \in \mathcal{T}} (\mathcal{F}(y), \nabla \mathbf{v})_\kappa + \sum_{\epsilon \in \mathcal{E}} (\mathcal{F}^\dagger(y^+, y^-, n), [\![\mathbf{v}]\!])_\epsilon = 0 \quad \forall \mathbf{v} \in V_h^p, \quad (3.2)$$

where (\cdot, \cdot) denotes the inner product, $\mathcal{F}^\dagger(y^+, y^-, n)$ is the numerical flux (taken to be the HLLC flux function [22]), and $[\![\cdot]\!]$ is the jump operator, given by $[\![\mathbf{v}]\!] = \mathbf{v}^+ - \mathbf{v}^-$ at interior interfaces and $[\![\mathbf{v}]\!] = \mathbf{v}^+$ at boundary interfaces. Throughout this work, a nodal basis is employed, such that the element-local polynomial approximation of the solution is expanded as

$$y_\kappa = \sum_{j=1}^{n_b} y_\kappa(x_j) \phi_j, \quad (3.3)$$

where n_b is the number of basis functions, $\{\phi_1, \dots, \phi_{n_b}\}$ is the set of basis functions, and $\{x_1, \dots, x_{n_b}\}$ is the set of node coordinates.

3.1 | Integration

The integrals in Equation (3.2) are computed using a quadrature-free approach [23, 24]. In the evaluation of the second and third integrals in Equation (3.2), the nonlinear convective flux is approximated as either

$$\mathcal{F}_f \approx \sum_{k=1}^{n_b} \mathcal{F}(y_\kappa(x_k)) \phi_k, \quad (3.4)$$

in the case of colocated integration, or

$$\mathcal{F}_f \approx \sum_{k=1}^{n_c} \mathcal{F}\left(\mathcal{P}(z(y_\kappa))|_{x_k}\right) \varphi_k, \quad (3.5)$$

in the case of overintegration, where $n_c > n_b$, $\{\varphi_1, \dots, \varphi_{n_c}\}$ is the corresponding set of basis functions, \mathcal{P} is a projection operator, and $z(y) : \mathbb{R}^m \rightarrow \mathbb{R}^m$ is a vector of intermediate state variables. In previous work [11], a number of options for \mathcal{P} and z were investigated in the context of mixtures of thermally perfect gases. Based on those results, we choose $\mathcal{P} = \Pi$, which is the L^2 -projection operator onto V_h^p , and $z = (v_1, \dots, v_d, P, C_1, \dots, C_{n_s})^T$. Other choices of \mathcal{P} , specifically the identity function (which corresponds to standard flux evaluation, i.e., $\sum_{k=1}^{n_c} \mathcal{F}(y_\kappa(x_k)) \varphi_k$) and interpolatory projection onto V_h^p , were not sufficiently robust in [11]. Note that in [11], $z = (v_1, \dots, v_d, P, T, Y_1, \dots, Y_{n_s-1})^T$ yielded the smallest deviations from pressure equilibrium; however, we find that this choice of z excessively modifies species concentrations, especially in Sections 4.4 and 4.5.

3.2 | Stabilization

Artificial viscosity is employed to stabilize the solution at discontinuous interfaces in Section 4.4. Note that we are primarily interested in contact interfaces in this work. Transcritical/supercritical flows with shocks are outside the scope of this study. The following dissipation term is added to the RHS of Equation (3.2) [25]:

$$\sum_{\kappa \in \mathcal{T}} (\mathcal{F}^{AV}(y, \nabla y), \nabla \mathbf{v})_\kappa, \quad (3.6)$$

where

$$\mathcal{F}^{AV}(y, \nabla y) = \nu_{AV}(y) \nabla y,$$

with $\nu_{AV} \geq 0$ denoting the artificial viscosity, which is computed as [10]

$$\nu_{AV} = (C_{AV} + S_{AV}) \left(\frac{h^2}{p+1} \left| \frac{\partial T}{\partial y} \cdot \frac{\mathcal{R}(y, \nabla y)}{T} \right| \right).$$

C_{AV} is a user-defined coefficient, S_{AV} is a sensor based on intra-element variations [26], and $\mathcal{R}(y, \nabla y)$ is the strong form of the residual (2.1). This type of artificial viscosity was found to effectively suppress spurious oscillations in the vicinity of flow-field discontinuities in multicomponent reacting flows [10, 27, 28]. Note, however, that the artificial-viscosity formulation described here is not the focus of this paper. Investigating other dissipative stabilization techniques, such as filtering and limiters, that may more effectively dampen nonlinear instabilities will be the subject of future work.

Finally, we employ a simple linear-scaling limiter [29, 27, 28] to help ensure well-behaved species concentrations, densities, and temperatures. It should be noted, however, that the formulation is not mathematically guaranteed to be positivity-preserving. Furthermore, this limiter by itself does not suppress small-scale instabilities.

4 | RESULTS

We consider four test cases. In the first one, which involves a sinusoidal density wave, we verify optimal convergence of the formulation. The second case is the one-dimensional advection of a nitrogen/n-dodecane thermal bubble, where we assess the ability of the methodology to maintain pressure equilibrium and solution stability. The third test is a two-dimensional version of the previous one. Curved elements are also considered. No additional dissipation is applied to the computations of the aforementioned test cases. The final two configurations involve the injection of an n-dodecane jet into a nitrogen chamber in two and three dimensions. All solutions are initialized using interpolation and then integrated in time using the third-order strong-stability-preserving Runge-Kutta scheme [30]. All simulations are performed using a modified version of the JENRE® Multiphysics Framework [10] that incorporates the extensions described in this work.

4.1 | Sinusoidal density wave

As in [5], we use this smooth flow problem to assess the grid convergence of the DG formulation (without artificial viscosity). A one-dimensional periodic domain $\Omega \in [0, 1]$ m is initialized as follows:

$$\begin{aligned} v_1 &= 100 \text{ m/s}, \\ Y_{N_2} &= 1, \\ \rho &= \frac{\rho_{\min} + \rho_{\max}}{2} - \frac{\rho_{\max} - \rho_{\min}}{2} \sin(2\pi x) \text{ kg/m}^3, \\ P &= 5 \text{ MPa}, \end{aligned}$$

where $\rho_{\min} = 56.9 \text{ kg/m}^3$ and $\rho_{\max} = 794 \text{ kg/m}^3$, which correspond to $T_{\max} = 300 \text{ K}$ and $T_{\min} = 100 \text{ K}$, respectively. Four element sizes are considered: h , $h/2$, $h/4$, and $h/8$, where $h = 0.04 \text{ m}$. We use a CFL number of 0.1 (based on the order-dependent linear-stability constraint) to minimize temporal error. The L^2 error at $t = 0.01 \text{ s}$, which corresponds to one period, is calculated in terms of the following normalized state variables:

$$\widehat{\rho v}_k = \frac{1}{\sqrt{\rho_r P_r}} \rho v_k, \quad \widehat{\rho e}_t = \frac{1}{P_r} \rho e_t, \quad \widehat{C}_i = \frac{R^0 T_r}{P_r} C_i,$$

where $T_r = 1000 \text{ K}$, $\rho_r = 1 \text{ kg}\cdot\text{m}^{-3}$, and $P_r = 101325 \text{ Pa}$ are reference values. The exact solution is simply the initial condition. We assess convergence with both colocated integration based on Gauss-Lobatto nodal sets and the overintegration strategy discussed in Section 3.1. Figure 4.1 presents results for $p = 1$ to $p = 3$. The dashed lines represent the theoretical convergence rates. The errors are slightly lower with the overintegration (3.5). Optimal order of accuracy is observed.

4.2 | One-dimensional advection of nitrogen/n-dodecane thermal bubble

This section presents results for the one-dimensional advection of a nitrogen/n-dodecane thermal bubble [5, 6]. In previous work [11], we computed this test case with the thermally perfect gas model. We are interested in how the proposed formulation performs here given the additional nonlinearities associated with the cubic equation of state and more complicated

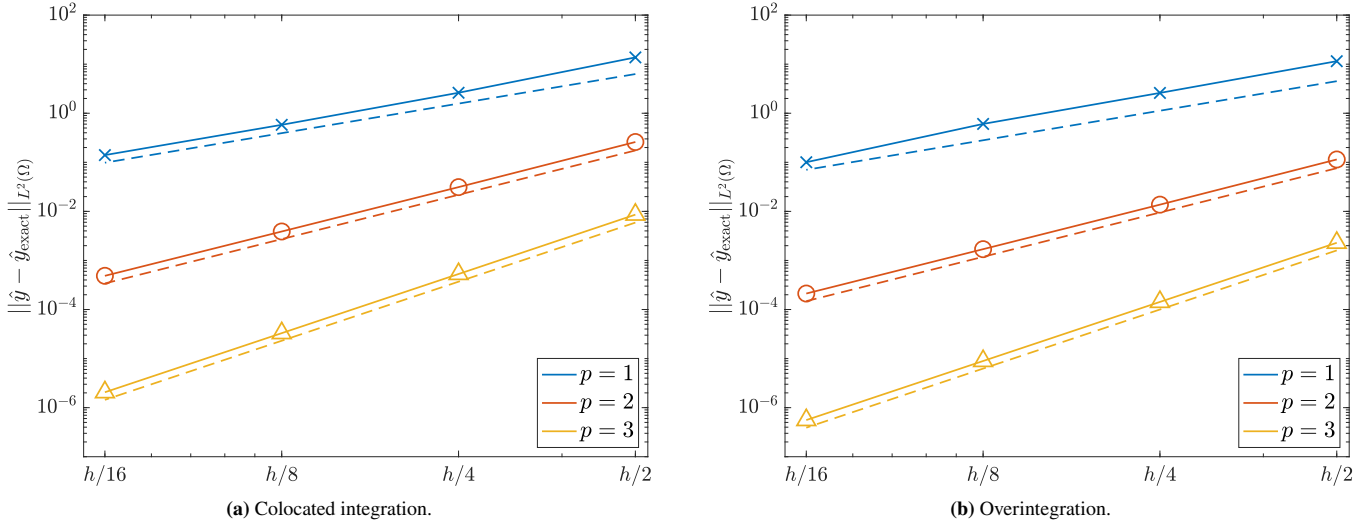


FIGURE 4.1 Convergence under grid refinement, with $h = 0.04$ m, for the one-dimensional sinusoidal density wave test. Figure 4.1a corresponds to colocated integration, and Figure 4.1b corresponds to the overintegration strategy discussed in Section 3.1. The L^2 error of the normalized state with respect to the exact solution is computed. The dashed lines represent the theroretical convergence rates.

thermodynamic relations. The initial conditions are given by

$$\begin{aligned}
 Y_{n\text{-C}_{12}\text{H}_{26}} &= \frac{1}{2} [1 - \tanh(25|x| - 5)], \\
 Y_{N_2} &= 1 - Y_{n\text{-C}_{12}\text{H}_{26}}, \\
 T &= \frac{T_{\min} + T_{\max}}{2} + \frac{T_{\max} - T_{\min}}{2} \tanh(25|x| - 5) \text{ K}, \\
 P &= 6 \text{ MPa}, \\
 v_1 &= 1 \text{ m/s}
 \end{aligned} \tag{4.1}$$

where $T_{\min} = 363$ K and $T_{\max} = 900$ K. The periodic domain is $\Omega = [-0.5, 0.5]$ m. The HLLC [22] flux function is employed. All solutions are advanced in time for ten periods with $\text{CFL} = 0.8$. Two separate grids with cell sizes of $h = 0.01$ m and $h = 0.005$ m are used. No artificial viscosity is employed.

Figure 4.2 presents $p = 1$, $p = 2$, and $p = 3$ solutions obtained with the overintegration (3.5). All solutions remain stable except for the $p = 1$ solution on the coarser grid. With standard overintegration, all solutions become unstable. $p = 0$ solutions on both meshes diverge as well. This illustrates the increased difficulty of maintaining solution robustness when real-fluid effects are considered. Despite noticeable deviations from pressure equilibrium in the coarser cases, they do not grow unbounded, as they would if standard integration were employed. As the polynomial order and/or number of cells increases, pressure equilibrium is better maintained and temperature is more accurately predicted. Note that despite the same number of degrees of freedom, the $p = 3$ solution on the coarser grid is more accurate than the $p = 1$ solution on the finer grid.

4.3 | Two-dimensional advection of nitrogen/n-dodecane thermal bubble

This flow configuration is a two-dimensional version of the previous test case, with initial conditions written as

$$\begin{aligned} Y_{n\text{-C}_{12}\text{H}_{26}} &= \frac{1}{2} \left[1 - \tanh \left(25 \sqrt{x_1^2 + x_2^2} - 5 \right) \right], \\ Y_{N_2} &= 1 - Y_{n\text{-C}_{12}\text{H}_{26}}, \\ T &= \frac{T_{\min} + T_{\max}}{2} + \frac{T_{\max} - T_{\min}}{2} \tanh \left(25 \sqrt{x_1^2 + x_2^2} - 5 \right) \text{ K}, \\ P &= 6 \text{ MPa}, \\ (v_1, v_2) &= (600, 0) \text{ m/s}, \end{aligned} \quad (4.2)$$

Note that the velocity is higher than in the previous test. In previous work [11], we investigated this high-velocity case in a one-dimensional, thermally perfect setting. The computational domain is $\Omega = (-0.5, 0.5) \text{ m} \times (-0.5, 0.5) \text{ m}$. The left and right boundaries are periodic, while symmetry conditions are imposed along the top and bottom boundaries. Gmsh [31] is used to generate an unstructured triangular grid with a characteristic cell size of $h = 0.01 \text{ m}$. Initial $p = 3$ density and pressure fields, superimposed by the grid, are displayed in Figure 4.3.

As in Section 4.2, the solutions are computed using the overintegration (3.5) and integrated in time for ten periods using a CFL number of 0.8. No artificial viscosity is employed. Figures 4.4, and 4.5 present the final density, temperature, pressure, and streamwise-velocity fields for $p = 2$ and $p = 3$ solutions, respectively. The solver diverges for $p = 1$ at these conditions. Note that $p = 1$, $p = 2$, and $p = 3$ with colocated integration also fail to maintain stability. The pressure and velocity ranges correspond to the actual respective minima and maxima in the corresponding solutions. Pressure oscillations are larger than in the one-dimensional case. Only small deviations from velocity equilibrium are present. In the $p = 2$ solution, discrepancies from the initial condition near the interfaces are observed. The $p = 3$ solution more accurately preserves the temperature and density profiles of the initial bubble and reduce deviations from pressure equilibrium.

Finally, we recompute the $p = 2$ and $p = 3$ cases using curved elements of quadratic geometric order. To generate the curved grid, high-order geometric nodes are inserted at the midpoints of the vertices of each element. At interior edges, the midpoint nodes are randomly perturbed by a distance up to $0.03h$. Figures 4.6 and 4.7 display the $p = 2$ and $p = 3$ results, respectively. The deviations from pressure and velocity equilibrium are slightly larger than for the straight-sided grid, but the density and temperature fields remain accurately predicted, suggesting that the employed overintegration strategy can maintain solution stability on curved grids.

4.4 | Two-dimensional n-dodecane jet

Next, we simulate two-dimensional injection of an n-dodecane jet into a quiescent nitrogen environment. Since phase separation is outside the scope of this work, we target the supercritical conditions considered by Rodriguez et al. [32]. The computational domain is a $5 \text{ mm} \times 2.5 \text{ mm}$ rectangular chamber, which is discretized by a fully unstructured triangular grid with a characteristic cell size of $h = 20 \mu\text{m}$. The total number of cells is 72,098. The domain is initialized with nitrogen at a pressure of 11.1 MPa and density of 37 kg/m^3 . The top and bottom boundaries are periodic, and the chamber pressure is specified at the outlet. The n-dodecane jet is injected at a streamwise velocity, pressure, and density of 200 m/s, 11.1 MPa, and 400 kg/m^3 , respectively, through a 0.1 mm-wide nozzle inlet located at the center of the left boundary. The remainder of the left boundary is a slip wall. No smoothing of the inflow is performed. Note that Rodriguez et al. [32] simulated this case with the PC-SAFT equation of state and viscous effects.

We compute $p = 1$, $p = 2$, and $p = 3$ solutions up to $t = 35 \mu\text{s}$ with a CFL number of 0.6. Figures 4.8, 4.9, and 4.10 display the density, temperature, pressure, and streamwise-velocity fields for $p = 1$, $p = 2$, and $p = 3$, respectively. Our results are qualitatively similar to those by Rodriguez et al. [32]. At these supercritical conditions, gas-like mixing is observed, instead of classical liquid-jet breakup into ligaments and droplets [33]. The boundary between the dense jet core and the ambient nitrogen appears as a sharp yet smooth transition. The dense core is shorter and thicker in the $p = 2$ and $p = 3$ solutions than in the $p = 1$ solution. Furthermore, the $p = 2$ and $p = 3$ solutions exhibit more vortical features and “finger-like” structures in the downstream region of the jet. Although spurious pressure oscillations can be observed in all cases, they remain relatively small and do not cause solver divergence. The density, temperature, and velocity fields are generally free from spurious artifacts.

4.5 | Three-dimensional n-dodecane jet

The final test case is a three-dimensional extension of that in Section 4.4, namely injection of a three-dimensional n-dodecane jet into a nitrogen environment. The computational domain is a cylindrical chamber of length 5 mm and radius 1.25 mm. The axis of the cylindrical domain is the x -axis. As in Section 4.4, the domain is initialized with nitrogen at a pressure of 11.1 MPa and density of 37 kg/m³. Slip-wall conditions are imposed along the walls of the cylinder, and the chamber pressure is specified at the outflow. The n-dodecane jet is injected at a streamwise velocity, pressure, and density of 200 m/s, 11.1 MPa, and 400 kg/m³, respectively, through a cylindrical nozzle inlet of radius 0.05 mm. The axis of the nozzle (not included in the computational domain) is the x -axis.

Gmsh [31] is used to generate an unstructured mesh with approximately 19 million tetrahedral cells. The characteristic cell size is specified to be $h = 10 \mu\text{m}$ within the truncated cone

$$C = \left\{ \sqrt{x_2^2 + x_3^2} \leq R_1 + \frac{R_2 - R_1}{L} x_1 \mid 0 \leq x_1 \leq L \right\},$$

where $R_1 = 0.075 \text{ mm}$, $R_2 = 0.95 \text{ mm}$, and $L = 4 \text{ mm}$. The mesh transitions to a characteristic cell size of $h = 0.5 \text{ mm}$ at the domain boundaries.

Figure 4.11 presents the density, temperature, pressure, and streamwise-velocity fields for a $p = 1$ solution at $t = 35 \mu\text{s}$. In order to reduce nonphysical instabilities at startup, the injection velocity is linearly ramped up from 0 m/s at $t = 0$ to 200 m/s at $t = 3 \mu\text{s}$. Compared to the two-dimensional results in Section 4.4, the three-dimensional dense jet core here is significantly narrower, and the finger-like structures are finer. Note, however, that periodicity is imposed at the top and bottom walls in Section 4.4. The boundary between the jet and the ambient nitrogen is sharp yet smooth. Figure 4.12 shows the density, temperature, pressure, and streamwise-velocity fields for a $p = 1$ solution at $t = 35 \mu\text{s}$. The $p = 2$ solution is started from the $p = 1$ solution at approximately $t = 3.35 \mu\text{s}$. Some spurious oscillations can be observed in both cases, although those in the $p = 1$ solution are more prominent at the interface. In addition, compared to the $p = 1$ solution, breakup of the jet occurs further upstream in the $p = 2$ solution, and the small-scale flow features are better resolved. Nevertheless, the $p = 1$ and $p = 2$ solutions are overall qualitatively similar. These results demonstrate the ability of the employed DG formulation to compute complex supercritical flows in three dimensions.

5 | CONCLUDING REMARKS

In this work, we presented a conservative DG methodology for the simulation of transcritical/supercritical, real-fluid flows without phase change. The methodology builds on a DG formulation originally developed to simulate multicomponent flows involving mixtures of thermally perfect gases [10, 11]. A key feature of the presented methodology is an overintegration strategy that employs an L^2 -projection of a set of intermediate variables onto the finite element test space when evaluating the flux, similar to techniques previously discussed in [13] and [12]. In the context of mixtures of thermally perfect gases, this overintegration strategy was found to effectively maintain approximate pressure equilibrium at smooth contact interfaces [11] without relying on dissipative stabilization in the form of artificial viscosity or limiting. Here, the ability of this strategy to maintain pressure equilibrium and solution stability in the presence of contact interfaces even with the added nonlinearities associated with a cubic equation of state and thermodynamic departure functions was of particular interest.

We applied the formulation to five test cases. In the first, which involved the advection of a sinusoidal density wave, optimal convergence was verified. In the second, we considered one-dimensional advection of a nitrogen/n-dodecane thermal bubble. In the thermally perfect case, both colocated integration and the employed overintegration strategy maintained solution stability over ten advection periods. However, with real-fluid effects accounted for, the former failed to prevent solver failure in nearly all considered simulations. In contrast, the latter maintained solution stability and small deviations from pressure equilibrium in all cases except the coarsest one. Increased resolution led to improved preservation of pressure equilibrium. The third test case involved a two-dimensional version of the previous configuration. Although spurious pressure oscillations were noticeably larger than in the one-dimensional case, the methodology was able to maintain solution stability on unstructured grids, including a grid with curved elements. Deviations from velocity equilibrium were generally small. The final test cases comprised two- and three-dimensional injection of an n-dodecane jet into a quiescent nitrogen environment, demonstrating the ability of the employed DG formulation to compute complex supercritical flows on unstructured simplicial grids.

Although these results are encouraging, there are still issues that should be addressed in future work. For example, the development of provably nonlinearly stable (e.g., positivity-preserving and entropy-stable) schemes for supercritical and transcritical flows would significantly improve robustness. However, the complex thermodynamics associated with this regime (especially in the case of mixtures) can introduce challenges such as loss of satisfaction of mathematical properties required by some conventional positivity-preserving schemes [29, 27, 28]. Recent work by Clayton et al. [34] represents an encouraging step in this direction. In addition, entropy-stable schemes rely on a mathematical entropy function that is convex with respect to the state [35, 36, 37], but common entropy functions that are valid in the ideal-gas case may lose convexity under certain conditions when real-fluid models are employed [38]. Another avenue for future work is the development of mathematically pressure-equilibrium-preserving schemes based on the conservative variables that do not rely on frozen thermodynamics (unlike the double-flux strategy). Recent work in this area has led to a number of promising formulations. For example, Bernades et al. [39] devised a kinetic-energy- and pressure-equilibrium-preserving finite-difference/finite-volume method, although total-energy conservation is still sacrificed. Terashima et al. [40] developed a method that is fully conservative and approximately pressure-equilibrium-preserving (note that the DG formulation here employs techniques that can reduce spurious pressure oscillations, but the pressure-equilibrium condition is not specifically invoked). However, mathematically guaranteeing both total-energy conservation and pressure-equilibrium preservation has remained elusive. Finally, in order to enable consideration of phase change in the transcritical regime, we will incorporate vapor-liquid-equilibrium calculations [21, 41] into the physical model.

ACKNOWLEDGMENTS

This work is sponsored by the Office of Naval Research through the Naval Research Laboratory 6.1 Computational Physics Task Area.

References

- [1] S. Jafari, Numerical modelling of transcritical turbulent jets using a tabulated real-fluid approach, Ph.D. thesis, Université Paris-Saclay (2022).
- [2] R. Abgrall, How to prevent pressure oscillations in multicomponent flow calculations: A quasi conservative approach, *Journal of Computational Physics* 125 (1) (1996) 150 – 160. doi:<https://doi.org/10.1006/jcph.1996.0085>.
- [3] S. Kawai, H. Terashima, H. Negishi, A robust and accurate numerical method for transcritical turbulent flows at supercritical pressure with an arbitrary equation of state, *Journal of Computational Physics* 300 (2015) 116–135.
- [4] R. Abgrall, S. Karni, Computations of compressible multifluids, *Journal of Computational Physics* 169 (2) (2001) 594 – 623. doi:<https://doi.org/10.1006/jcph.2000.6685>.
- [5] P. C. Ma, Y. Lv, M. Ihme, An entropy-stable hybrid scheme for simulations of transcritical real-fluid flows, *Journal of Computational Physics* 340 (2017) 330–357.
- [6] B. Boyd, D. Jarrahdashi, A diffuse-interface method for reducing spurious pressure oscillations in multicomponent transcritical flow simulations, *Computers & Fluids* 222 (2021) 104924.
- [7] Z. Wang, K. Fidkowski, R. Abgrall, F. Bassi, D. Caraeni, A. Cary, H. Deconinck, R. Hartmann, K. Hillewaert, H. Huynh, N. Kroll, G. May, P.-O. Persson, B. van Leer, M. Visbal, High-order CFD methods: Current status and perspective, *International Journal for Numerical Methods in Fluids* (2013). doi:[10.1002/fld.3767](https://doi.org/10.1002/fld.3767).
- [8] T. Hitz, M. Heinen, J. Vrabec, C.-D. Munz, Comparison of macro-and microscopic solutions of the Riemann problem I. Supercritical shock tube and expansion into vacuum, *Journal of Computational Physics* 402 (2020) 109077.
- [9] L. D. Gryngarten, S. Menon, A generalized approach for sub-and super-critical flows using the local discontinuous Galerkin method, *Computer Methods in Applied Mechanics and Engineering* 253 (2013) 169–185.
- [10] R. F. Johnson, A. D. Kercher, A conservative discontinuous Galerkin discretization for the chemically reacting Navier-Stokes equations, *Journal of Computational Physics* 423 (2020) 109826. doi:[10.1016/j.jcp.2020.109826](https://doi.org/10.1016/j.jcp.2020.109826).

- [11] E. J. Ching, R. F. Johnson, A. D. Kercher, A note on reducing spurious pressure oscillations in fully conservative discontinuous Galerkin simulations of multicomponent flows, arXiv preprint arXiv:2310.17792 (2023).
- [12] K. Bando, Towards high-performance discontinuous Galerkin simulations of reacting flows using Legion, Ph.D. thesis, Stanford University (2023).
- [13] N. Franchina, M. Savini, F. Bassi, Multicomponent gas flow computations by a discontinuous Galerkin scheme using L2-projection of perfect gas EOS, Journal of Computational Physics 315 (2016) 302–322.
- [14] D.-Y. Peng, D. B. Robinson, A new two-constant equation of state, Industrial & Engineering Chemistry Fundamentals 15 (1) (1976) 59–64.
- [15] B. J. McBride, S. Gordon, M. A. Reno, Coefficients for calculating thermodynamic and transport properties of individual species (1993).
- [16] B. J. McBride, M. J. Zehe, S. Gordon, NASA Glenn coefficients for calculating thermodynamic properties of individual species (2002).
- [17] J. F. Ely, H. Hanley, Prediction of transport properties. 1. viscosity of fluids and mixtures, Industrial & Engineering Chemistry Fundamentals 20 (4) (1981) 323–332.
- [18] J. F. Ely, H. Hanley, Prediction of transport properties. 2. thermal conductivity of pure fluids and mixtures, Industrial & Engineering Chemistry Fundamentals 22 (1) (1983) 90–97.
- [19] K. G. Harstad, R. S. Miller, J. Bellan, Efficient high-pressure state equations, AIChE journal 43 (6) (1997) 1605–1610.
- [20] P. C. Ma, Modeling of turbulent mixing and combustion at transcritical conditions, Ph.D. thesis, Stanford University (2018).
- [21] P. C. Ma, H. Wu, D. T. Banuti, M. Ihme, On the numerical behavior of diffuse-interface methods for transcritical real-fluids simulations, International Journal of Multiphase Flow 113 (2019) 231–249.
- [22] E. Toro, Riemann solvers and numerical methods for fluid dynamics: A practical introduction, Springer Science & Business Media, 2013.
- [23] H. Atkins, C. Shu, Quadrature-free implementation of discontinuous Galerkin methods for hyperbolic equations, ICASE Report 96-51, 1996, Tech. rep., NASA Langley Research Center, nASA-CR-201594 (August 1996).
- [24] H. L. Atkins, C.-W. Shu, Quadrature-free implementation of discontinuous Galerkin method for hyperbolic equations, AIAA Journal 36 (5) (1998) 775–782.
- [25] R. Hartmann, T. Leicht, Higher order and adaptive DG methods for compressible flows, in: H. Deconinck (Ed.), VKI LS 2014-03: 37th Advanced VKI CFD Lecture Series: Recent developments in higher order methods and industrial application in aeronautics, Dec. 9-12, 2013, Von Karman Institute for Fluid Dynamics, Rhode Saint Genèse, Belgium, 2014.
- [26] E. Ching, Y. Lv, P. Gnoffo, M. Barnhardt, M. Ihme, Shock capturing for discontinuous Galerkin methods with application to predicting heat transfer in hypersonic flows, Journal of Computational Physics 376 (2019) 54–75.
- [27] E. J. Ching, R. F. Johnson, A. D. Kercher, Positivity-preserving and entropy-bounded discontinuous Galerkin method for the chemically reacting, compressible Euler equations. Part I: The one-dimensional case, Journal of Computational Physics (2024) 112881.
- [28] E. J. Ching, R. F. Johnson, A. D. Kercher, Positivity-preserving and entropy-bounded discontinuous Galerkin method for the chemically reacting, compressible Euler equations. Part II: The multidimensional case, Journal of Computational Physics (2024) 112878.
- [29] X. Zhang, C.-W. Shu, On positivity-preserving high order discontinuous Galerkin schemes for compressible Euler equations on rectangular meshes, Journal of Computational Physics 229 (23) (2010) 8918–8934.
- [30] S. Gottlieb, C. Shu, E. Tadmor, Strong stability-preserving high-order time discretization methods, SIAM review 43 (1) (2001) 89–112.

- [31] C. Geuzaine, J.-F. Remacle, Gmsh: a three-dimensional finite element mesh generator with built-in pre- and post-processing facilities, International Journal for Numerical Methods in Engineering (79(11)) (2009) 1310–1331.
- [32] C. Rodriguez, P. Koukouvinis, M. Gavaises, Simulation of supercritical diesel jets using the PC-SAFT EoS, The Journal of Supercritical Fluids 145 (2019) 48–65.
- [33] B. Chehroudi, D. Talley, W. Mayer, R. Branam, J. Smith, A. Schik, M. Oschwald, Understanding injection into high pressure supercritical environments, in: Fifth International Symposium on Liquid Space Propulsion, Long Life Combustion Devices Technology, NASA Marshall Space Flight Center, Huntsville, Alabama, October, 2003, pp. 27–30.
- [34] B. Clayton, J.-L. Guermond, M. Maier, B. Popov, E. J. Tovar, Robust second-order approximation of the compressible Euler equations with an arbitrary equation of state, Journal of Computational Physics 478 (2023) 111926.
- [35] A. Harten, P. D. Lax, B. v. Leer, On upstream differencing and Godunov-type schemes for hyperbolic conservation laws, SIAM review 25 (1) (1983) 35–61.
- [36] T. Chen, C.-W. Shu, Entropy stable high order discontinuous Galerkin methods with suitable quadrature rules for hyperbolic conservation laws, Journal of Computational Physics 345 (2017) 427–461.
- [37] J. Chan, On discretely entropy conservative and entropy stable discontinuous Galerkin methods, Journal of Computational Physics 362 (2018) 346–374.
- [38] V. Giovangigli, L. Matuszewski, Mathematical modeling of supercritical multicomponent reactive fluids, Mathematical Models and Methods in Applied Sciences 23 (12) (2013) 2193–2251.
- [39] M. Bernades, L. Jofre, F. Capuano, Kinetic-energy-and pressure-equilibrium-preserving schemes for real-gas turbulence in the transcritical regime, Journal of Computational Physics 493 (2023) 112477.
- [40] H. Terashima, N. Ly, M. Ihme, Approximately pressure-equilibrium-preserving scheme for fully conservative simulations of compressible multi-species and real-fluid interfacial flows, Available at SSRN 4747391 (2024).
- [41] H. Zhang, N. Srinivasan, S. Yang, In situ adaptive tabulation of vapor-liquid equilibrium solutions for multi-component high-pressure transcritical flows with phase change, Journal of Computational Physics 500 (2024) 112752.
- [42] K. Wark, Advanced Thermodynamics for Engineers, McGraw-Hill New York, 1995.
- [43] A. Piña-Martinez, R. Privat, I. K. Nikolaidis, I. G. Economou, J.-N. Jaubert, What is the optimal activity coefficient model to be combined with the translated-consistent Peng–Robinson equation of state through advanced mixing rules? cross-comparison and grading of the Wilson, UNIQUAC, and NRTL a^E models against a benchmark database involving 200 binary systems, Industrial & Engineering Chemistry Research 60 (47) (2021) 17228–17247.
- [44] C. Zhang, H. Li, X. Zhang, L. Ju, Linear and unconditionally energy stable schemes for the multi-component two-phase diffuse interface model with Peng–Robinson equation of state, Communications in Computational Physics 26 (4) (2019).

How to cite this article: E. J. Ching and R. F. Johnson (2024), Conservative discontinuous Galerkin method for supercritical, real-fluid flows, *IJNMF*,

APPENDIX

A THERMODYNAMIC RELATIONS

This section provides additional information on the thermodynamic relations for a generic cubic equation of state written as

$$P = \frac{\hat{R}T}{\hat{v} - b} - \frac{a\alpha}{(\hat{v} + \delta_1 b)(\hat{v} + \delta_2 b)}, \quad (\text{A1})$$

where δ_1 and δ_2 are constants that depend on the specific equation of state. Further details can be found in [5, 20]. For mixtures, the attractive and repulsive parameters (also known as the energy and co-volume parameters, respectively) are computed as

$$a\alpha = \sum_{i=1}^{n_s} \sum_{j=1}^{n_s} X_i X_j a_{ij} \alpha_{ij},$$

$$b = \sum_{i=1}^{n_s} X_i b_i,$$

and the critical mixture conditions for temperature, pressure, molar volume, and acentric factor are given by

$$T_{c,ij} = \sqrt{T_{c,i} T_{c,j}} (1 - k_{ij}),$$

$$P_{c,ij} = Z_{c,ij} \frac{\hat{R} T_{c,ij}}{\hat{v}_{c,ij}},$$

$$\hat{v}_{c,ij} = \frac{1}{8} \left(\hat{v}_{c,i}^{1/3} + \hat{v}_{c,j}^{1/3} \right)^3,$$

$$\omega_{ij} = \frac{\omega_i + \omega_j}{2},$$

respectively, with $(\cdot)_i$ denoting the corresponding property of the i th species. k_{ij} is the binary interaction parameter, which is assumed to be zero [20].

For the Peng-Robinson equation of state, $\delta_1 = 1 + \sqrt{2}$, $\delta_2 = 1 - \sqrt{2}$, and

$$a_{ij} = 0.45724 \frac{\hat{R}^2 T_{c,ij}^2}{P_{c,ij}},$$

$$\alpha_{ij} = \left[1 + c_{ij} \left(1 - \sqrt{\frac{T}{T_{c,ij}}} \right) \right]^2,$$

$$b_i = 0.07780 \frac{\hat{R} T_{c,ij}}{P_{c,ij}},$$

$$c_{ij} = 0.37464 + 1.54226 \omega_{ij} - 0.26992 \omega_{ij}^2.$$

In addition, we have

$$\frac{d\alpha_{ij}}{dT} = -c_{ij} \sqrt{\frac{\alpha_{ij}}{TT_{c,ij}}}$$

and

$$\frac{d^2\alpha_{ij}}{dT^2} = \frac{c_{ij}^2}{2TT_{c,ij}} + \frac{c_{ij}}{2} \sqrt{\frac{\alpha_{ij}}{T^3 T_{c,ij}}}.$$

Unless otherwise specified, the remainder of this section applies to generic cubic equations of state of the form (A1).

Thermodynamic quantities are evaluated as the sum of the corresponding mixture-averaged ideal-gas value (assuming a thermally perfect gas) and a departure function [42]. The ideal-gas values can be computed based on polynomial fits [15, 16] and are denoted $(\cdot)^{(I)}$. The molar internal energy is given by

$$\hat{u}(T, \hat{v}, X_i) = \hat{u}^{(I)}(T, X_i) + \int_{\hat{v}}^{\infty} \left[P - T \left(\frac{\partial P}{\partial T} \right)_{\hat{v}, X_i} \right] d\hat{v}$$

$$= \hat{u}^{(I)}(T, X_i) + K_1 \left[a\alpha - T \left(\frac{\partial a\alpha}{\partial T} \right)_{X_i} \right],$$

where

$$K_1 = \int_{\hat{v}}^{\infty} \frac{d\hat{v}}{(\hat{v} + \delta_1 b)(\hat{v} + \delta_2 b)} = \frac{1}{(\delta_1 - \delta_2) b} \ln \left(\frac{\hat{v} + \delta_2 b}{\hat{v} + \delta_1 b} \right).$$

The molar enthalpy can then be computed as

$$\hat{h} = \hat{u} + P\hat{v}.$$

In this work, where we employ the Peng-Robinson equation of state (i.e., $\delta_1 = 1 + \sqrt{2}$ and $\delta_2 = 1 - \sqrt{2}$), K_1 is calculated as

$$K_1 = \frac{1}{2\sqrt{2}b} \ln \left[\frac{\hat{v} + (1 - \sqrt{2})b}{\hat{v} + (1 + \sqrt{2})b} \right], \quad \hat{v} = \max \{ \hat{v}, b \},$$

to prevent undefined behavior and for consistency with the constraint $\hat{v} > b$, which is motivated by the fact that for a pure fluid, b represents the molar volume as the pressure tends to infinity (i.e., the co-volume) [43]. In addition, the Helmholtz free energy of a homogeneous mixture is undefined for $\hat{v} \leq b$ [44]. Enforcing this behavior directly on the solution in a rigorous manner while maintaining accuracy is beyond the scope of this study.

The molar entropy is given by

$$\begin{aligned} \hat{s}(T, \hat{v}, X_i) &= \hat{s}^{(I)}(T, \hat{v}, X_i) + \int_{\hat{v}}^{\infty} \left[\rho R - \left(\frac{\partial P}{\partial T} \right)_{\hat{v}, X_i} \right] d\hat{v} \\ &= \hat{s}^{(I)}(T, \hat{v}, X_i) + \hat{R} \ln \frac{\hat{v} - b}{\hat{v}} - K_1 \left(\frac{\partial a\alpha}{\partial T} \right)_{X_i}, \end{aligned}$$

where $R = \hat{R}/\bar{W}$ is the specific gas constant, with \bar{W} denoting the mixture molecular mass, which is defined as

$$\bar{W} = \frac{\rho}{\sum_{i=1}^{n_s} C_i} = \sum_{i=1}^{n_s} X_i W_i.$$

The molar heat capacities at constant volume and constant pressure are evaluated as

$$\hat{c}_v = \left(\frac{\partial \hat{u}}{\partial T} \right)_{\hat{v}, X_i} = \hat{c}_v^{(I)}(T, X_i) - K_1 T \left(\frac{\partial^2 a\alpha}{\partial T^2} \right)_{X_i}$$

and

$$\hat{c}_p = \left(\frac{\partial \hat{h}}{\partial T} \right)_{P, X_i} = \hat{c}_p^{(I)}(T, X_i) - \hat{R} - K_1 T \left(\frac{\partial^2 a\alpha}{\partial T^2} \right)_{X_i} - T \frac{(\partial P / \partial T)_{\hat{v}, X_i}^2}{(\partial P / \partial \hat{v})_{T, X_i}^2},$$

respectively. Finally, the square of the speed of sound is given by

$$c^2 = \left(\frac{\partial P}{\partial \rho} \right)_{s, X_i} = \frac{\gamma}{\rho \kappa_T},$$

where γ is the specific heat ratio and κ_T is the isothermal compressibility, written as

$$\kappa_T = -\frac{1}{\hat{v}} \left(\frac{\partial \hat{v}}{\partial P} \right)_{T, X_i}.$$

The partial derivatives in the above thermodynamic relations can be expressed as follows:

$$\begin{aligned} \left(\frac{\partial a\alpha}{\partial T} \right)_{X_i} &= \sum_{i=1}^{n_s} \sum_{j=1}^{n_s} X_i X_j a_{ij} \frac{d\alpha_{ij}}{dT}, \\ \left(\frac{\partial^2 a\alpha}{\partial T^2} \right)_{X_i} &= \sum_{i=1}^{n_s} \sum_{j=1}^{n_s} X_i X_j a_{ij} \frac{d^2 \alpha_{ij}}{dT^2}, \\ \left(\frac{\partial P}{\partial T} \right)_{\hat{v}, X_i} &= \frac{\hat{R}}{\hat{v} - b} - \frac{(\partial a\alpha / \partial T)_{X_i}}{(\hat{v} + \delta_1 b)(\hat{v} + \delta_2 b)}, \\ \left(\frac{\partial P}{\partial \hat{v}} \right)_{T, X_i} &= -\frac{\hat{R} T}{(\hat{v} - b)^2} - \frac{a\alpha [2\hat{v} + (\delta_1 + \delta_2)b]}{(\hat{v} + \delta_1 b)^2 (\hat{v} + \delta_2 b)^2}. \end{aligned}$$

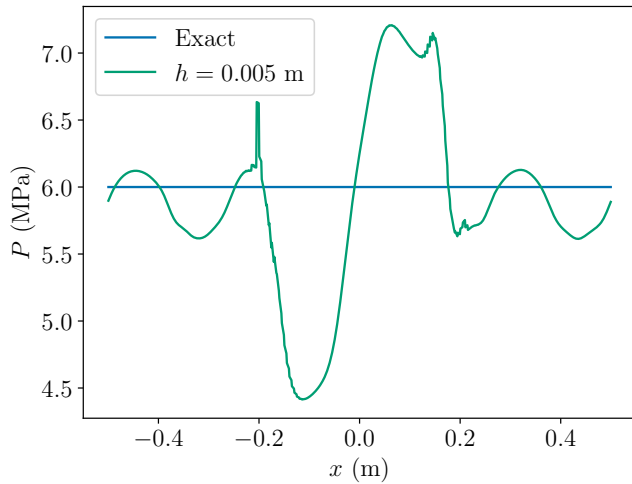
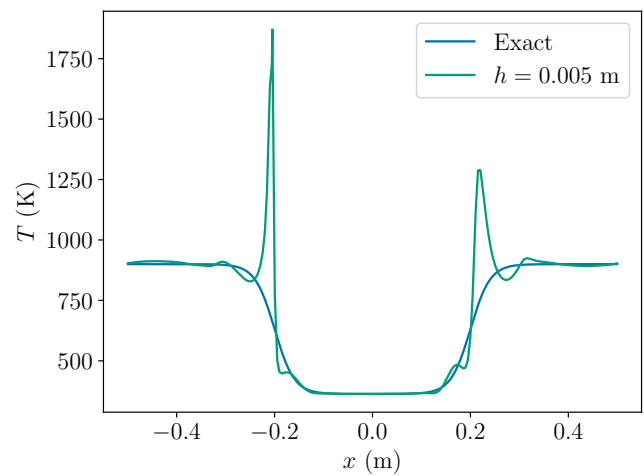
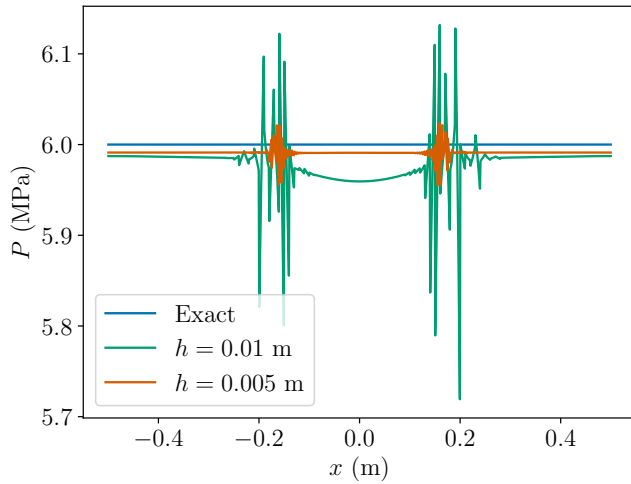
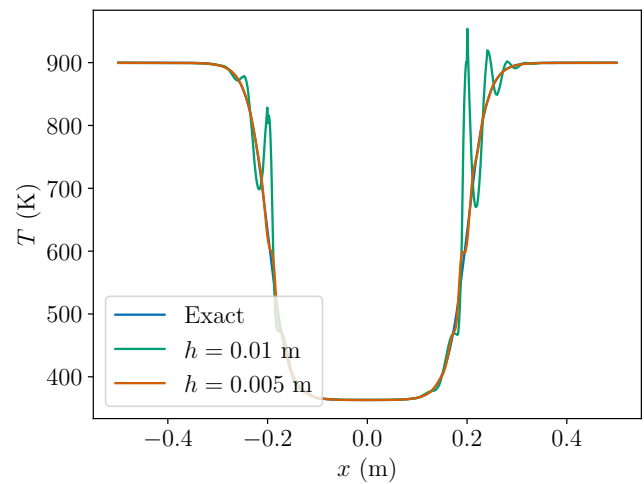
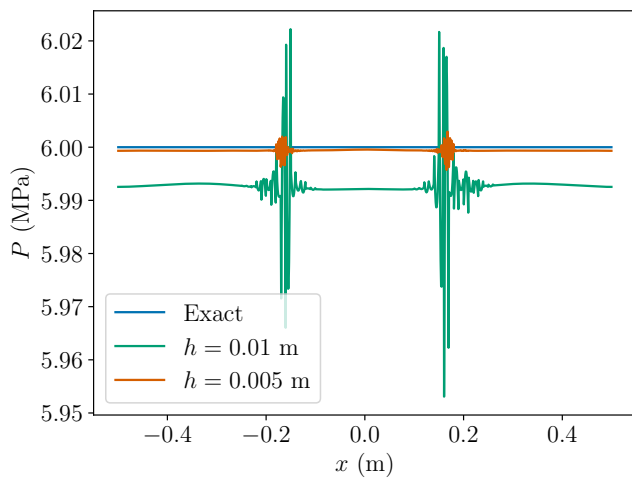
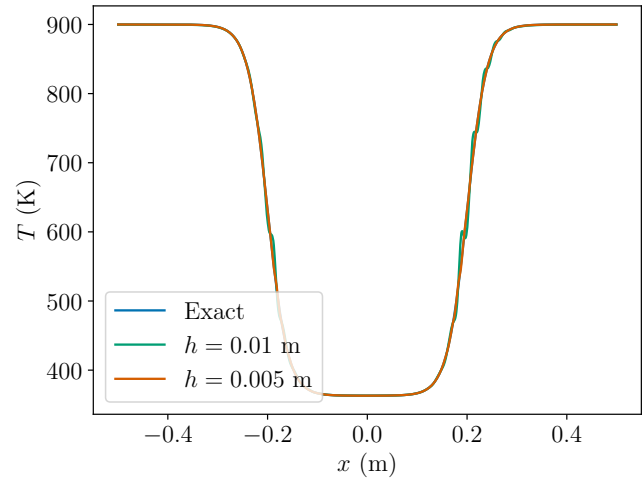
(a) Pressure, $p = 1$.(b) Temperature, $p = 1$.(c) Pressure, $p = 2$.(d) Temperature, $p = 2$.(e) Pressure, $p = 3$.(f) Temperature, $p = 3$.

FIGURE 4.2 $p = 1$, $p = 2$, and $p = 3$ solutions to the one-dimensional advection of a nitrogen/n-dodecane thermal bubble after ten periods. The overintegration (3.5) is employed. Pressure and temperature profiles obtained with cell sizes of $h = 0.02$ m and $h = 0.01$ m. However, the $p = 1$, $h = 0.02$ m solution diverges and is therefore not shown.

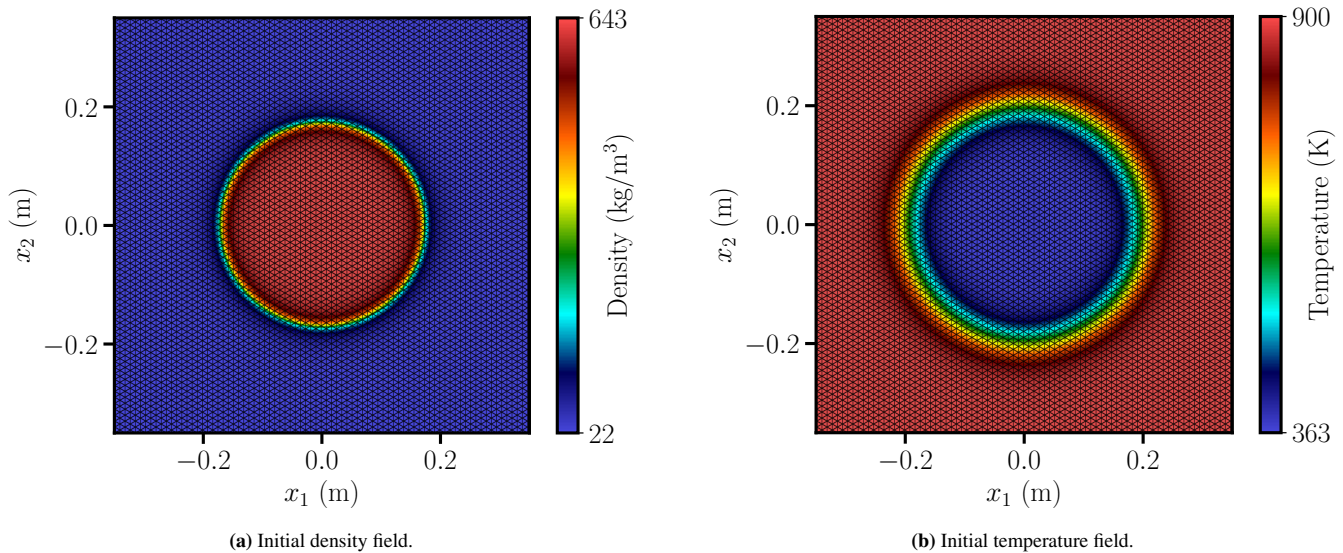


FIGURE 4.3 Initial $p = 3$ density and pressure fields, superimposed by the grid, for the two-dimensional advection of a nitrogen/n-dodecane thermal bubble.

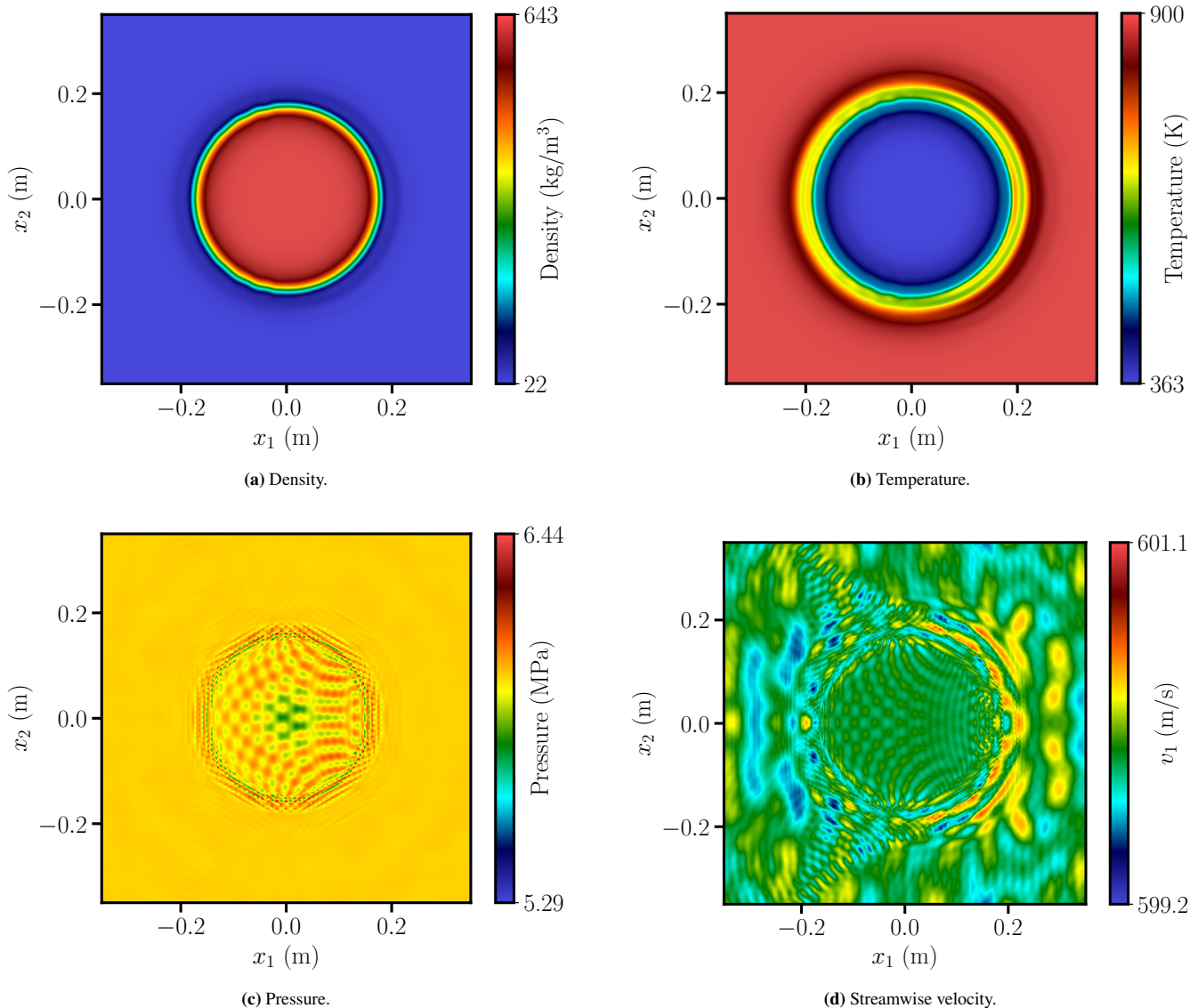


FIGURE 4.4 $p = 2$ solution to two-dimensional advection of a nitrogen/n-dodecane thermal bubble after ten periods. The colorbar minima and maxima for the pressure and velocity fields are the respective global minima and maxima.

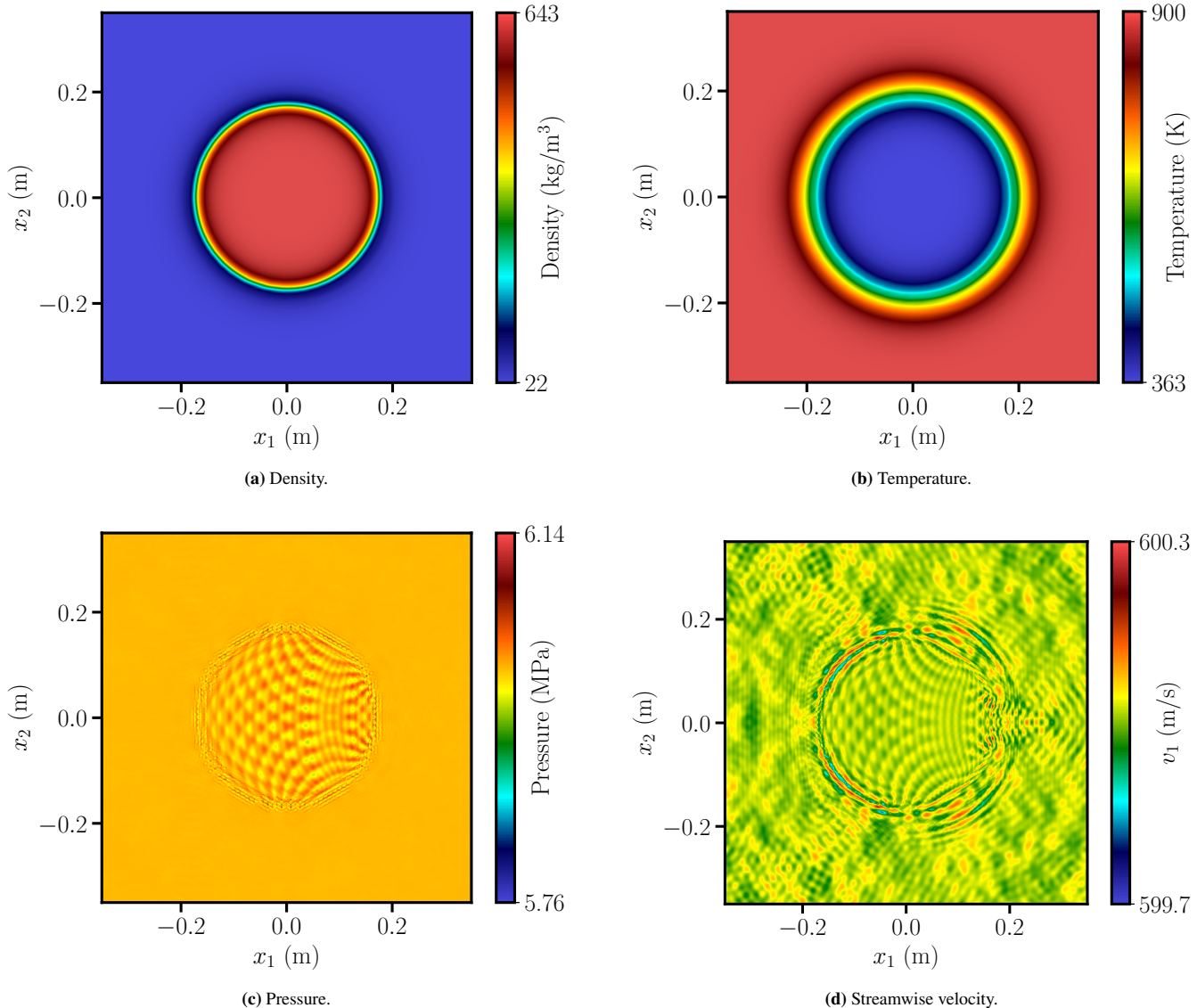


FIGURE 4.5 $p = 3$ solution to two-dimensional advection of a nitrogen/n-dodecane thermal bubble after ten periods. The colorbar minima and maxima for the pressure and velocity fields are the respective global minima and maxima.

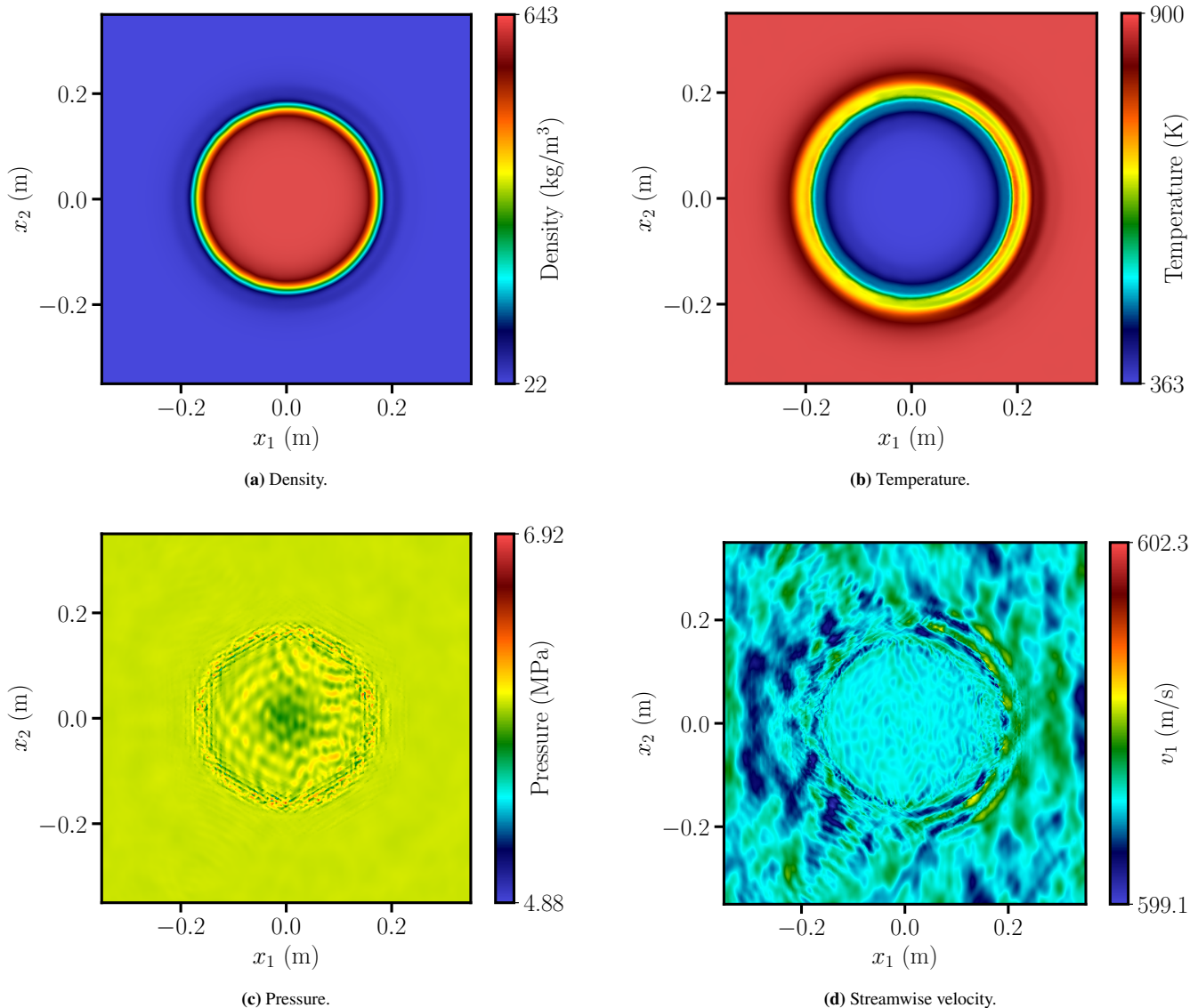


FIGURE 4.6 $p = 2$ solution to two-dimensional advection of a nitrogen/n-dodecane thermal bubble after ten periods on a curved grid. The colorbar minima and maxima for the pressure and velocity fields are the respective global minima and maxima.

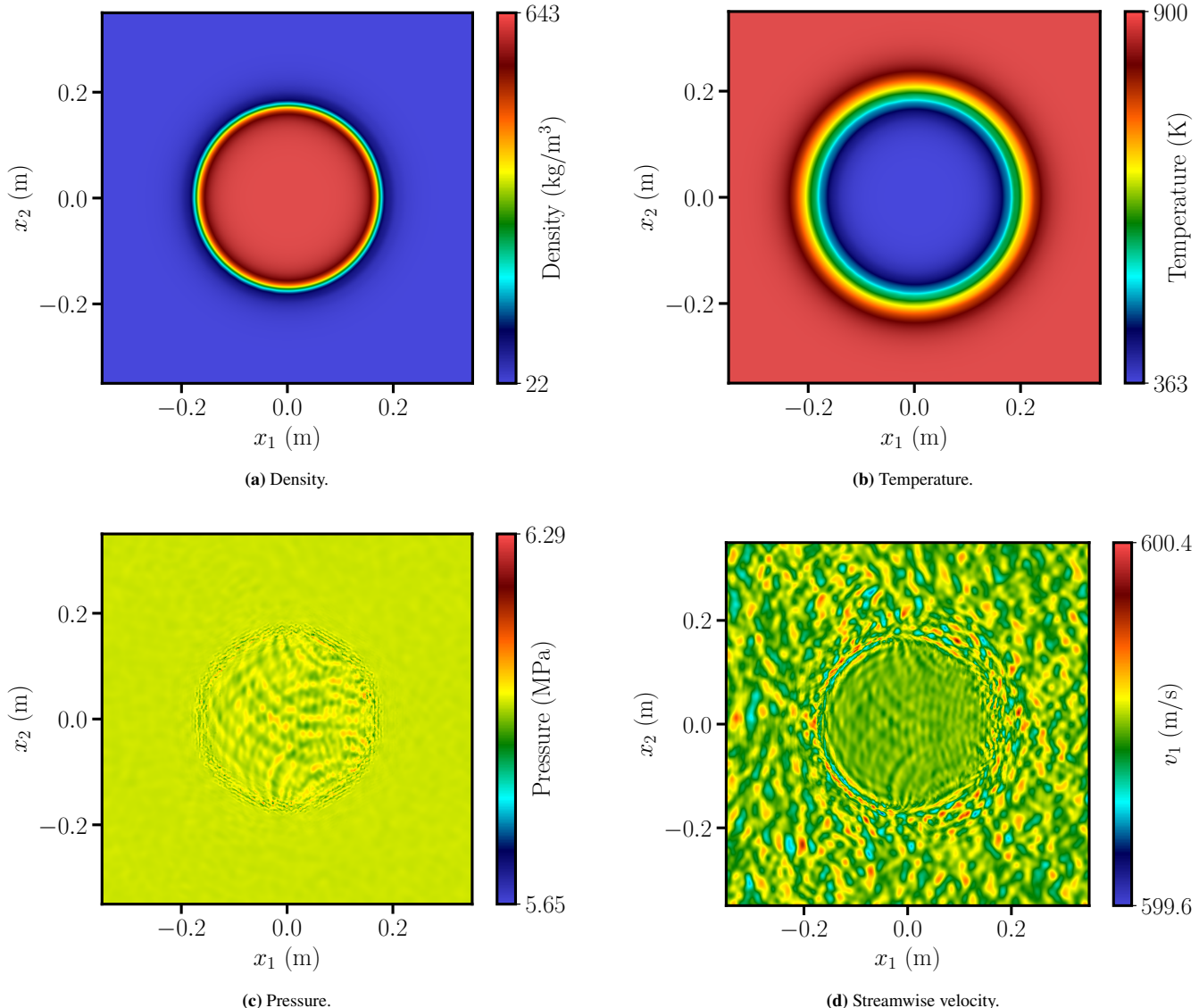


FIGURE 4.7 $p = 3$ solution to two-dimensional advection of a nitrogen/n-dodecane thermal bubble after ten periods on a curved grid. The colorbar minima and maxima for the pressure and velocity fields are the respective global minima and maxima.

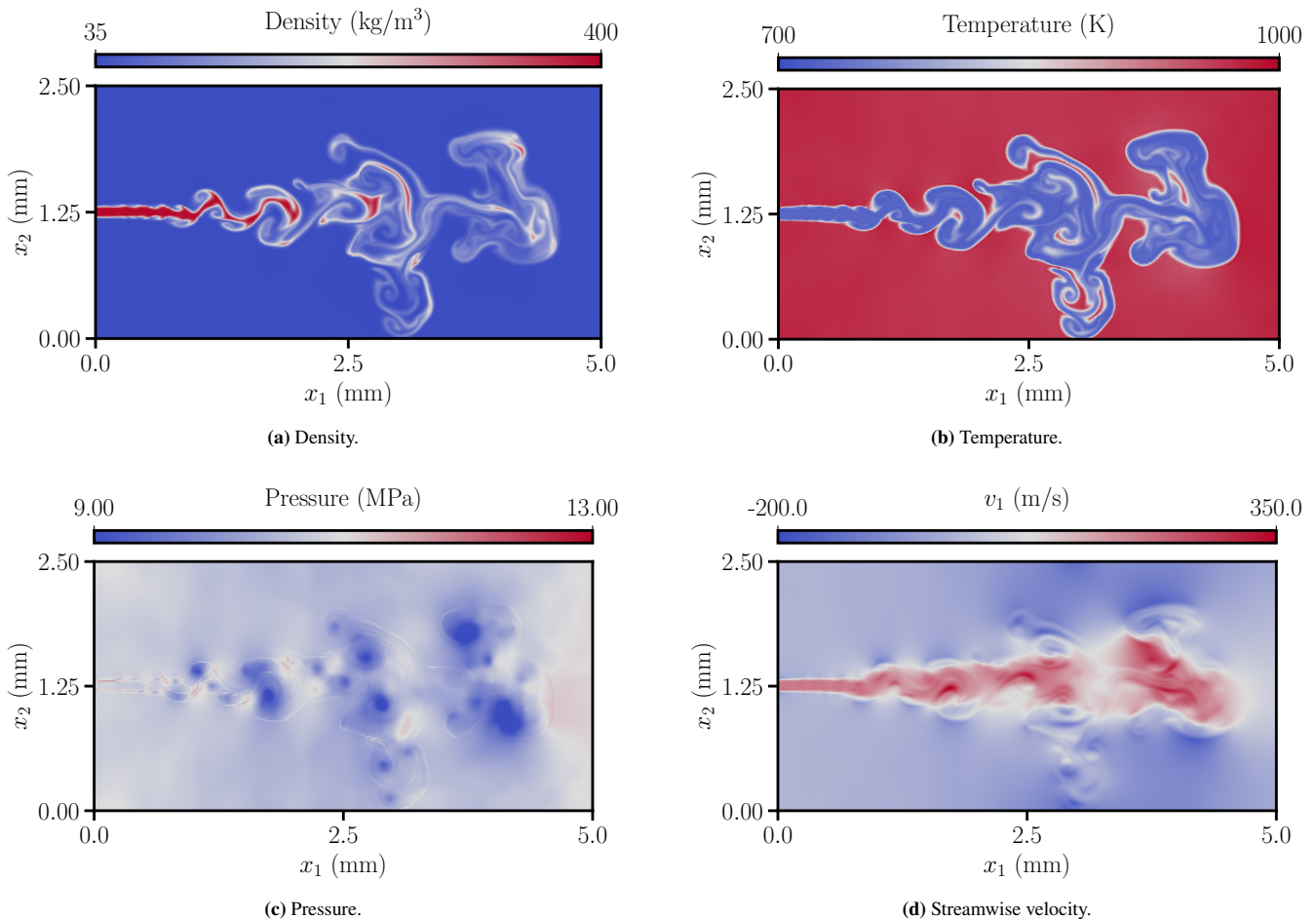


FIGURE 4.8 $p = 1$ solution to two-dimensional injection of an n-dodecane jet into a quiescent nitrogen environment at $t = 35 \mu\text{s}$.

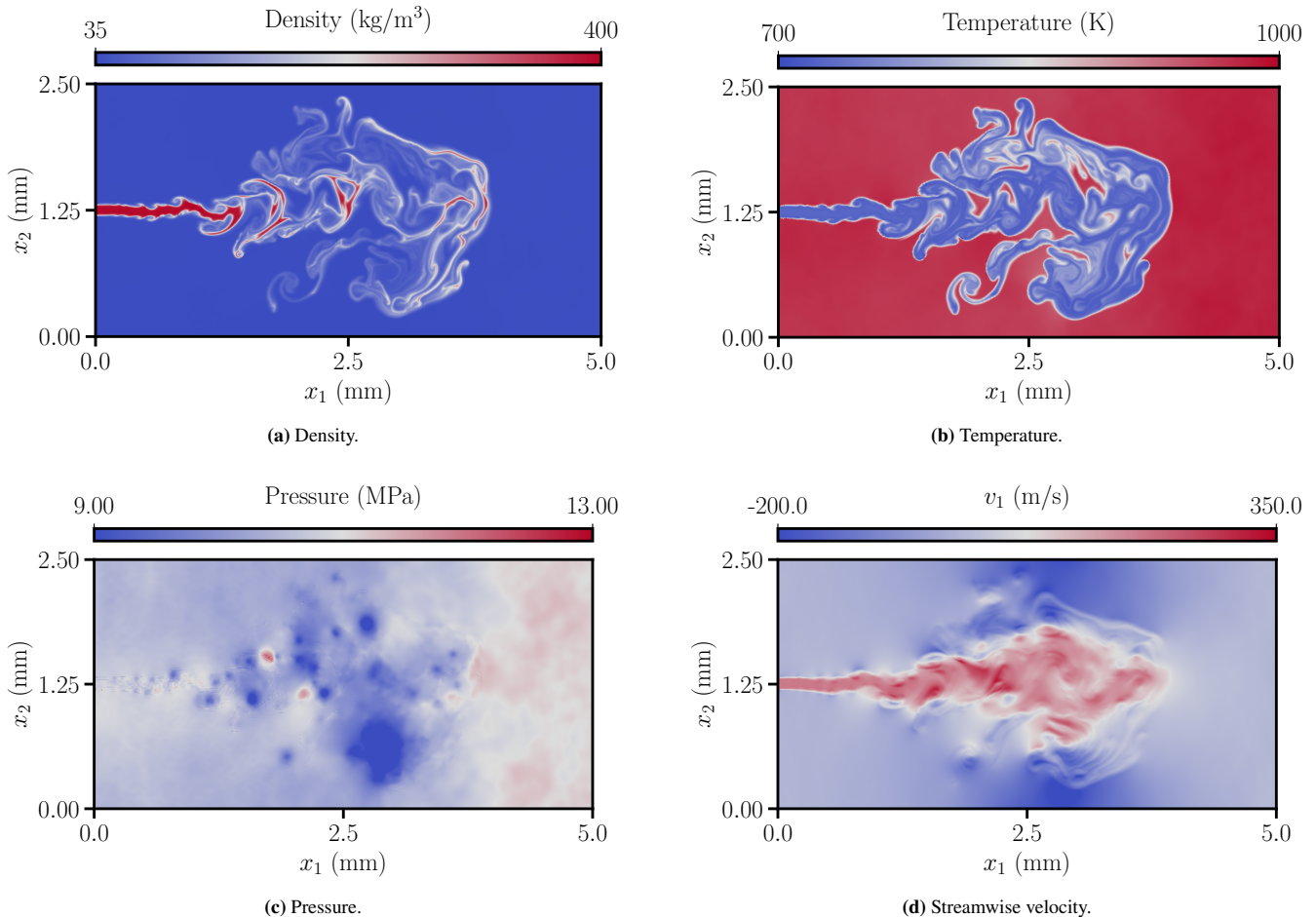


FIGURE 4.9 $p = 2$ solution to two-dimensional injection of an n-dodecane jet into a quiescent nitrogen environment at $t = 35 \mu\text{s}$.

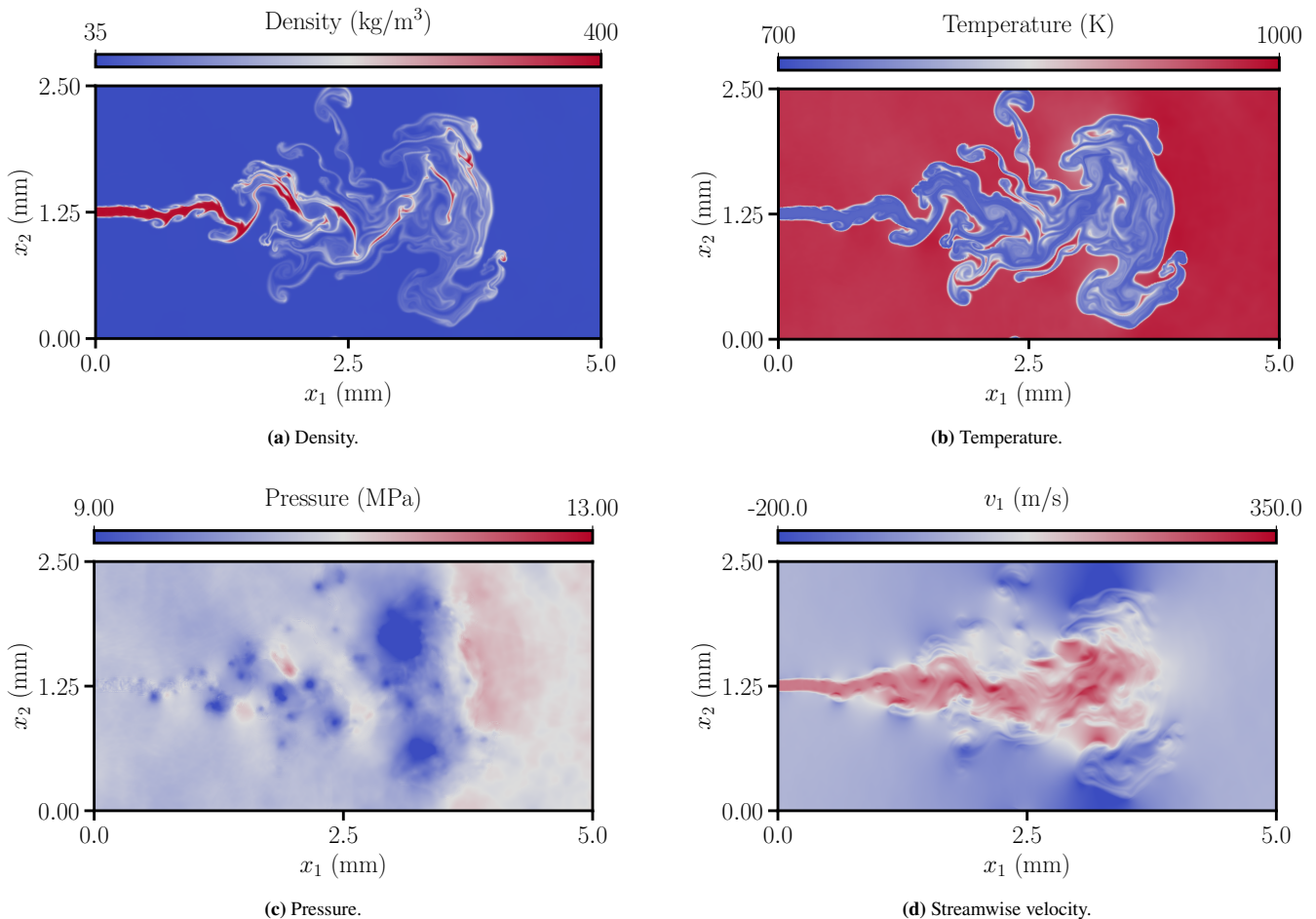


FIGURE 4.10 $p = 3$ solution to two-dimensional injection of an n-dodecane jet into a quiescent nitrogen environment at $t = 35 \mu\text{s}$.

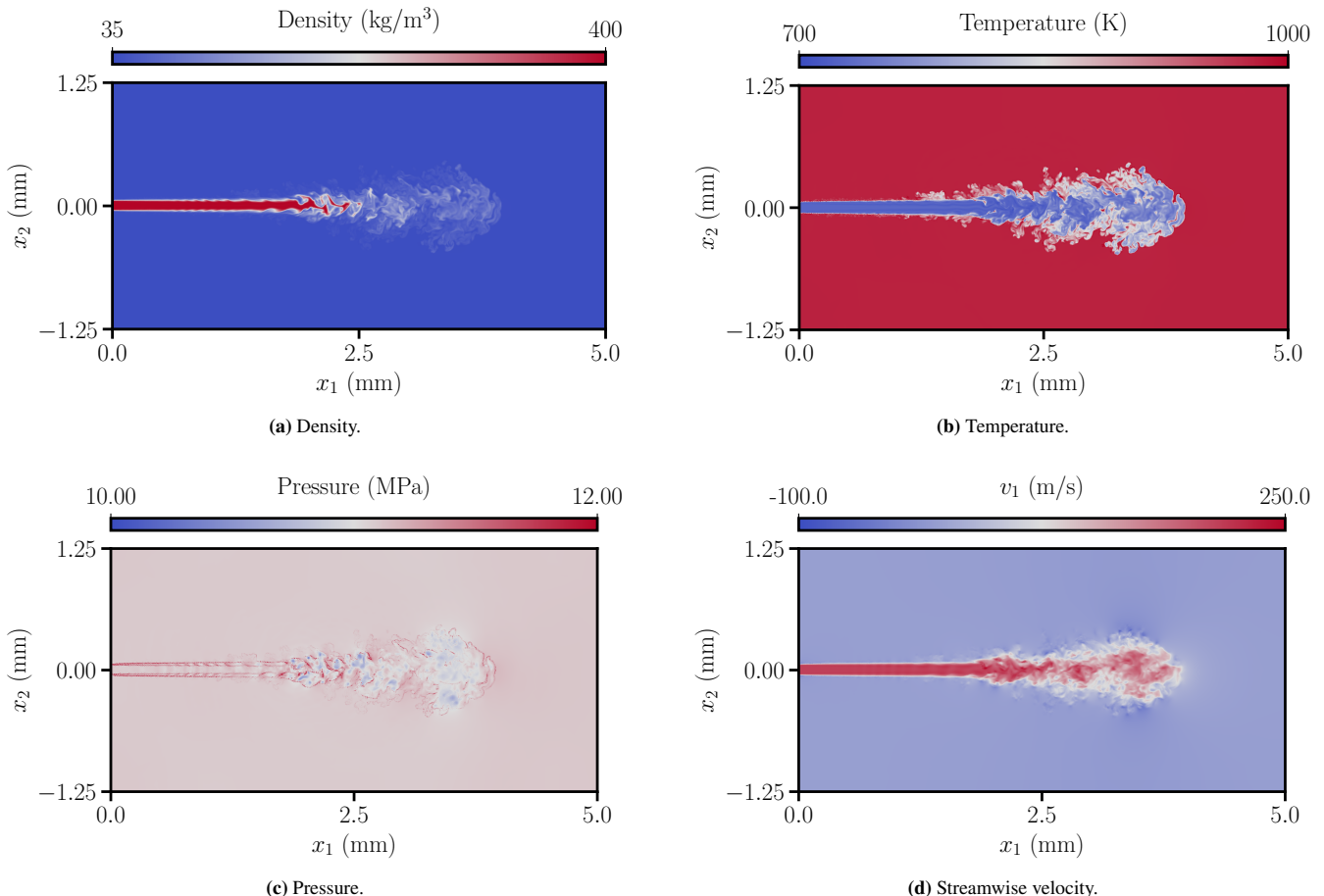


FIGURE 4.11 $p = 1$ solution to three-dimensional injection of an n-dodecane jet into a quiescent nitrogen environment at $t = 35 \mu\text{s}$.

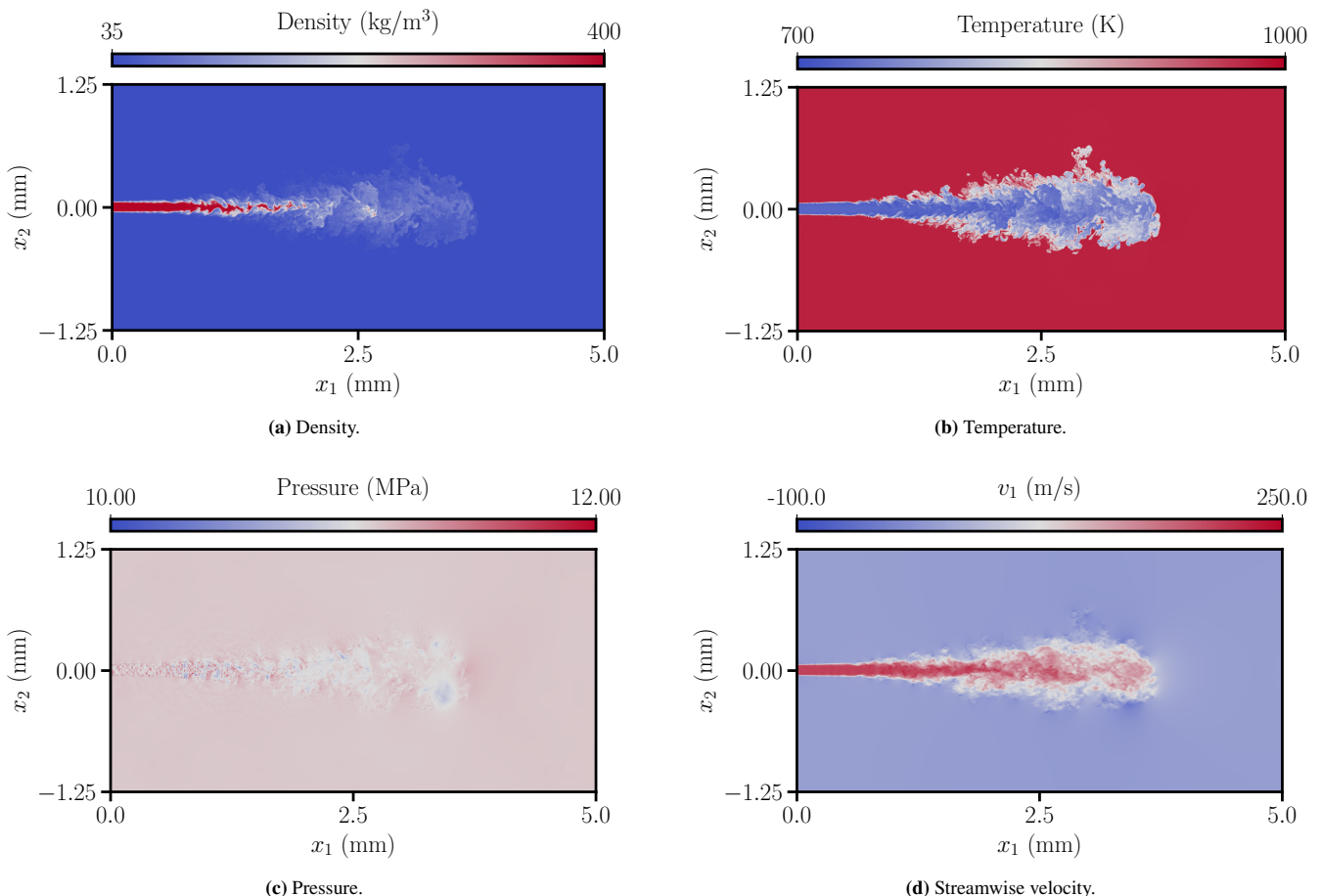


FIGURE 4.12 $p = 2$ solution to three-dimensional injection of an n-dodecane jet into a quiescent nitrogen environment at $t = 35 \mu\text{s}$.